



www.acsami.org Research Article

Critical Coupling of Visible Light Extends Hot-Electron Lifetimes for H₂O₂ Synthesis

Daniel E. Willis, Mohammad M. Taheri, Orhan Kizilkaya, Tiago R. Leite, Laibao Zhang, Tochukwu Ofoegbuna, Kunlun Ding, James A. Dorman, Jason B. Baxter, and Kevin M. McPeak*



Cite This: ACS Appl. Mater. Interfaces 2020, 12, 22778-22788



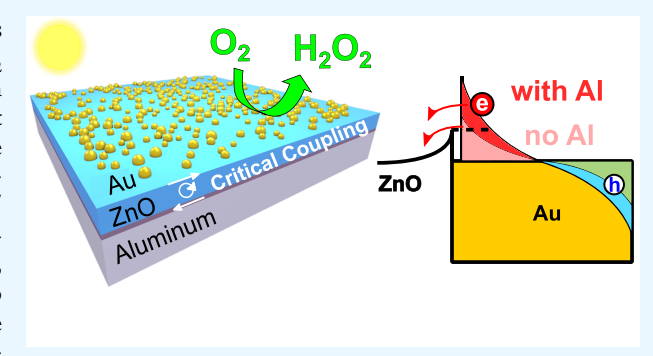
ACCESS

Metrics & More

Article Recommendations

s Supporting Information

ABSTRACT: Devices driven by above-equilibrium "hot" electrons are appealing for photocatalytic technologies, such as in situ $\rm H_2O_2$ synthesis, but currently suffer from low (<1%) overall quantum efficiencies. Gold nanostructures excited by visible light generate hot electrons that can inject into a neighboring semiconductor to drive electrochemical reactions. Here, we designed and studied a metal–insulator–metal (MIM) structure of Au nanoparticles on a ZnO/TiO₂/Al film stack, deposited through room-temperature, lithography-free methods. Light absorption, electron injection efficiency, and photocatalytic yield in this device are superior in comparison to the same stack without Al. Our device absorbs >60% of light at the Au localized surface plasmon resonance (LSPR) peak near 530 nm—a 5-fold enhancement in Au absorption due to critical coupling to an



Al film. Furthermore, we show through ultrafast pump—probe spectroscopy that the Al-coupled samples exhibit a nearly 5-fold improvement in hot-electron injection efficiency as compared to a non-Al device, with the hot-electron lifetimes extending to >2 ps in devices photoexcited with fluence of 0.1 mJ cm $^{-2}$. The use of an Al film also enhances the photocatalytic yield of H_2O_2 more than 3-fold in a visible-light-driven reactor. Altogether, we show that the critical coupling of Al films to Au nanoparticles is a low-cost, lithography-free method for improving visible-light capture, extending hot-carrier lifetimes, and ultimately increasing the rate of in situ H_2O_2 generation.

KEYWORDS: hot electrons, photocatalysis, plasmonics, critical coupling, visible light, ultrafast, pump-probe spectroscopy

1. INTRODUCTION

The efficient capture and conversion of sunlight into usable energy is essential for life on earth—generally, through photosynthesis, and commercially, through an assortment of photovoltaic, photocatalytic, and photothermal technologies. 1-7 Plasmonic metal (Au, Ag, Cu, and Al) nanostructures can absorb a significant fraction of visible light and generate "hot" electrons—with internal energies above the Fermi level-primarily through interband transitions and Landau damping.8-11 Hot electrons can transfer from metals to adjoined semiconductors, mitigating carrier recombination and facilitating further electrochemical reactions. 12-15 The overall efficiency of hot-electron devices is limited by the efficiencies of individual processes, including (A) light absorption, (B) energy conversion to hot electrons, (C) transport and injection of carriers into a neighboring material, and (D) work attained by the injected carriers. 16-18 Researchers have taken a variety of approaches to improve these processes; however, the overall quantum efficiency of hot-electron devices is frequently below 1%. 2,3,7,19-21 The primary bottlenecks to hot-electron device performance are typically attributed to hot-electron generation and injection

phenomena. On the basis of previous work,^{6,9} we hypothesize that enhancing the electromagnetic field confinement at a metal—semiconductor interface will increase light absorption as well as hot-electron generation and lifetime and ultimately improve the efficiency of the hot-electron device.

A promising route to enhance both light absorption and the electromagnetic field confinement in plasmonic nanostructures is to implement them in a metal-insulator-metal (MIM) framework, with a thin (20–150 nm) dielectric spacer between the nanostructures and a metal film tuned to achieve critical coupling of incident light within the optical cavity. Principally, the radiative and nonradiative decay rates of resonant photonic energy fed into the MIM system are matched, which leads to near-perfect light absorption over a broad spectral range. ^{20,26,27} Critical coupling is notably

Received: January 19, 2020 Accepted: April 27, 2020 Published: April 27, 2020





different from other MIM designs with ultrathin (<10 nm) spacers implemented for near-field coupling or thicker (>150 nm) spacers that collect visible light through Fabry-Perot internal reflections. ^{28,29} For critical coupling, small (<30 nm) metal nanostructures are often used to absorb large fractions of light, with dimensionality less than the mean free path of hot electrons. 5,11,30 All told, critically coupled devices are orders of magnitude thinner than commercial, Si-based light absorbers and less sensitive to the illumination polarization or angle of incidence than Fabry-Perot structures. 26,27,31 Researchers have implemented expensive nanofabrication techniques to create well patterned, size-controlled plasmonic structures for fundamental studies, ^{24,32,33} but photocatalytic applications beyond the laboratory require efficient hot-electron devices fabricated via low-cost methods and materials.

In this work, we enhance electromagnetic fields in Au nanoparticles at a ZnO interface through critical coupling with an Al film and explore the impact on device absorption, hotelectron injection, and photocatalytic activity. Our plasmonic device, shown in Figure 1a, is designed as a MIM structure of

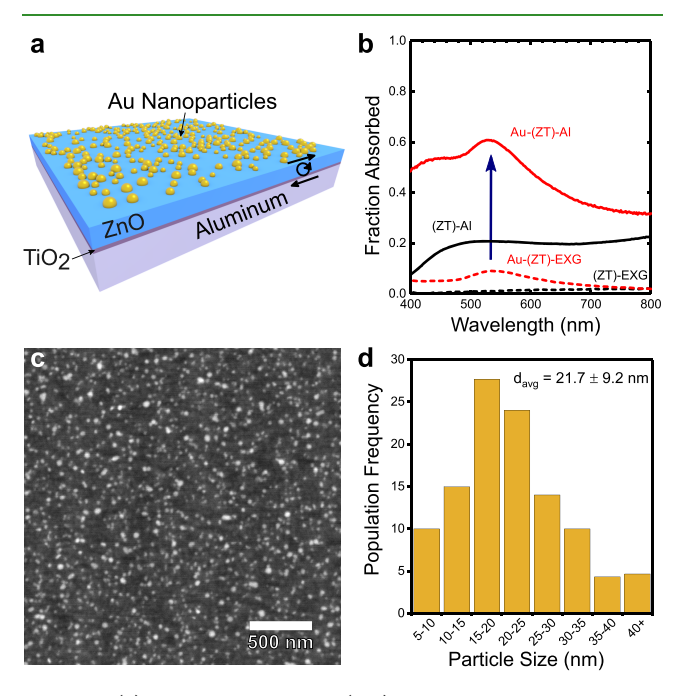


Figure 1. (a) Schematic of the Au-(ZT)-Al optical cavity, designed to increase visible-light absorbance in the Au nanoparticles. (b) Absorbance spectra for samples, including controls fabricated without Au and Al for comparison. (c) Backscatter SEM image of the Au-(ZT)-Al surface. (d) Respective size distribution of Au nanoparticles determined by analysis of multiple images with ImageJ software.

Au nanoparticles on a ZnO thin film with a TiO2-capped Al reflective layer, denoted Au-(ZT)-Al. We utilize ZnO as a dielectric spacer due to its high electrical conductivity, low crystallization temperature, and conduction band position. The Al film provides excellent visible light reflection at significantly lower material costs than other common MIM mirrors, such as Au—as of this writing, the cost of Al is ~25 000 times cheaper than that of Au. 34,35 With our device, we measured a broad 7.4× increase in absorption across the visible spectrum (400– 650 nm) through the implementation of the Al back reflector, with a 5-fold enhancement at the absorption maximum (530 nm) attributed to the localized surface plasmon resonance (LSPR) of the Au nanostructures. Furthermore, pump-probe

spectroscopy revealed the ultrafast dynamics of charge carrier generation and electron transfer. 36,37 We measured the accumulation of electrons in the ZnO conduction band upon visible (450 nm $< \lambda < 700$ nm) photoexcitation of Au and showed a nearly 5-fold improvement in the injection efficiency in Al-backed devices compared to those without Al. We also observed a significant extension of the electron-phonon coupling time in Al-backed samples over a range of pump fluences, suggesting that some of the Al-induced improvement in the hot-electron collection may be attributed to higher effective electron temperatures and slower thermalization. Altogether, we provide evidence that the efficiency of hotelectron transfer from Au nanostructures to ZnO can be improved by critically coupling the Au nanostructures to an inexpensive Al mirror. The improvement in hot-electron collection also resulted in higher photoactivity of the Au-(ZT)-Al sample compared to Au-(ZT)-glass controls in the generation of H₂O₂ in near-aqueous solutions. These efficiency enhancements open the door for the use of low-cost materials and lithography-free fabrication as a route to improving visiblelight-driven hot-electron devices.

2. RESULTS AND DISCUSSION

2.1. Fabrication and Characterization of MIM Structures. We designed Au-(ZT)-Al structures to increase the electric field confinement in Au nanoparticles at the Au/ ZnO interface and thereby improve the injection of hot electrons into ZnO. We thermally evaporated an optically thick (300 nm) layer of Al onto a Corning Eagle XG (EXG) glass substrate with a 5 nm chromium adhesion layer. Furthermore, we capped the Al layer with a thin, pinhole free layer of TiO₂ through atomic layer deposition (ALD), which suppressed thermomechanical stresses and catalytic reactivity in the underlying Al. 38,39 Spectroscopic ellipsometry confirmed the presence of ~10 nm of TiO₂ (Figures S1 and S2). We also prepared control samples without Al but with thin TiO2 on EXG. After TiO₂ deposition, we spun and annealed a ZnO sol-gel to form a crystalline thin film of ZnO. All ZnO films in this study were 50 nm thick unless otherwise noted. Through X-ray diffraction, we confirmed the wurtzite structure of ZnO, with mean domain sizes calculated by the Scherrer equation of \sim 12 nm (eq S1 and Figure S8).^{40,41}

To achieve room-temperature synthesis of Au nanostructures, we made use of the direct bandgap semiconductor nature of ZnO and performed Au photodeposition. We followed a method based on studies by Waclawik et al.,⁴² with adjustments to the concentration of HAuCl₄, pulse time of UV light, and convective shaking parameters applied to form Au nanostructures of below 30 nm in diameter (Figure S9). The absorption of the Au-(ZT)-Al device, as measured with a spectrophotometer equipped with an integrating sphere, was an average of 7.4× higher than controls without Al over the visible-light (400-650 nm) spectrum, as shown in Figure 1b. Scanning electron microscopy (SEM) images of the sample surface provided details of the Au particles, as shown in Figure 1c. We also collected electron micrographs of the surfaces with a backscatter detector, which allowed us to better distinguish Au from the ZnO background and more accurately estimate Au nanoparticle size and distribution (Figures S11-S13). We analyzed multiple images with thousands of particles in ImageJ to quantify the particle size distribution (see Figure 1d), which confirmed an Au particle size distribution of 21.7 \pm 9.2 nm with a surface coverage of ~15.6%. Sacrificial samples were

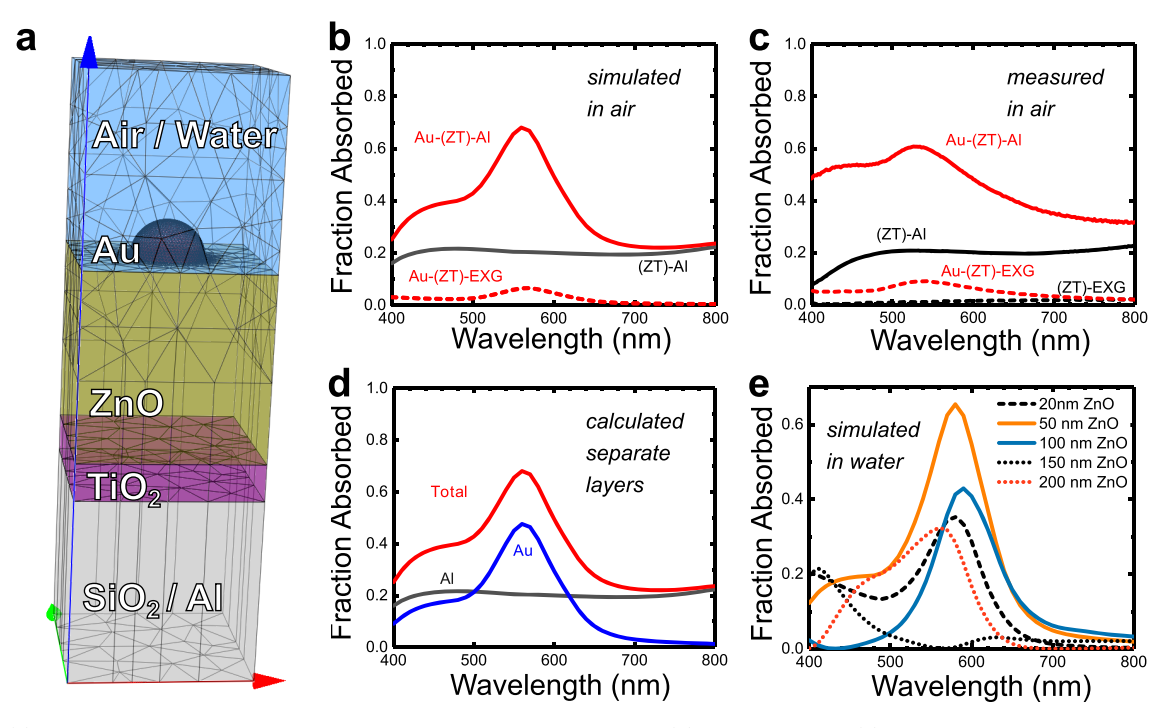


Figure 2. (a) Mesh used in finite element method simulation with JCMsuite. (b) Simulated and (c) measured absorbance for Au-(ZT)-Al structures and controls. (d) Absorbance of individual materials in the simulated data set is separated to estimate the increase in absorbance for Au NPs specifically. (e) Simulations of our device in water with varying ZnO thicknesses. We attribute the absorbance enhancement near 50 nm ZnO to critical coupling (solid lines as opposed to that of near-field coupling effects (dashed line) or Fabry—Perot interferences (dotted lines) simulated with thinner or thicker oxide spacers layers, respectively).

etched with aqua regia, and the diluted effluents were examined through inductively coupled plasma optical emission spectroscopy (ICP-OES) to quantify a mass of 5.92 \pm 0.4 μ g Au per cm² surface area on our samples, which corresponds to a mass loading of ~17% on the underlying ZnO (Figure S14).

2.2. Simulation and Measurement of Maximum **Optical Absorption.** To determine the best dielectric spacer thickness to maximize the Au absorption in our MIM device, we performed full-field finite element method simulations of idealized three-dimensional structures using JCMsuite software. The Au nanoparticle was modeled as a perfect 20 nm diameter hemisphere on a flat ZnO surface isolated on a 50 nm × 50 nm domain with the assumption that particles were spaced far enough apart to avoid near-field interactions, 43 as supported by SEM images of particle size and density and shown in Figure 2a. The dielectric constants of all film layers (Au, Al, TiO2, and ZnO) were calculated by using modified Cauchy and B-Spline models from data collected with a J.A. Woollam RC2 ellipsometer (tabulated data available in the Supporting Information). The dielectric properties for the EXG substrate were pulled from a previous spectroscopic ellipsometry study by Cushman et al. 44 The initial simulations were based on a ZnO thickness of 50 nm to achieve a spacer thickness of $d \approx \lambda_0/4n$, which is often used to invert the phase of light upon reflection in optical cavities and create destructive interference to minimize reflection.²⁴ For our ZnO, the index of refraction is ~2.0 near the Au nanostructure resonant wavelength $\lambda_0 = 530$ nm. We also accounted for the additional thickness of TiO2 and the native oxide on the Al layer. The simulated absorption spectra of the Au-(ZT)-Al structures in air, along with controls lacking Au or Al, are shown in Figure 2b. The Au LSPR peak in these simulations is around 550 nm in samples with and without Al present. While the ZnO/TiO2

layers do not absorb light above \sim 420 nm in wavelength, the Al backing accounts for a near-constant 20% absorption of visible light, with a gradual increase in absorption up to \sim 830 nm due to the Al interband transition at \sim 1.5 eV.

We compared the measured optical absorption of our samples to the simulated absorption spectra. Results in Figure 2c overlap very well with the simulated absorbance profiles from our simulations, with a few key differences. For one, the LSPR peak for Au is blue-shifted in our experimental data, owing mainly to a different medium of incidence than simulations (air vs water). To a lesser degree, Au clusters formed during photodeposition may lead to deviations in the Au nanoparticle geometry (vs simulations), resulting in slight changes in optical properties. ^{11,13} Our samples also exhibit greater absorption in the spectra <500 nm, an energy range in which Au interband transitions are prominent. The intensity of Au interband transitions are also associated with particle morphology. ^{46,47}

Using JCMsuite, we calculated the fraction of light absorbed by each layer in ideal Au-(ZT)-Al structures. These simulations (Figure 2d) confirm that only Au nanoparticles and the Al film in our system absorb visible light. On the basis of these calculations, we estimated an \sim 5-fold increase in the LSPR absorbance of our actual Au nanostructures through critical coupling with the Al film. Similar improvements in structural absorption enhancement have been observed in MIM structures, though typically Au is used as the optical mirror. 20,22 Our results demonstrate similar enhancements with lower cost Al films.

To assess the ideal spacer thickness for maximizing absorbance of Au nanostructures, we performed further simulations that supported the original assumption that ${\sim}50$ nm ZnO was the ideal thickness. We varied the ZnO

thicknesses while leaving all other layers unchanged in the simulations. The optical properties of MIMs are strongly dependent on the spacer thicknesses, shown by the simulation results in Figure 2e, as well as extended simulation and experimental data in Figures S6 and S7. These simulations were performed in water to more accurately predict sample absorption during photocatalytic studies (section 2.5), while the experimental absorbance data were collected in air. From this data and previous literature studies, we identify three regimes of spacer thickness and their effect on absorption in the Au nanoparticles. When the spacer thickness is <20 nm, the metals are in close proximity, and near-field coupling dominates. Multiple groups have studied these near-field effects in Au-spacer-Au structures and physically measured antiparallel currents in the metals. ^{28,48,49} In our structures, however, near-field effects did not provide a maximal absorption for the Au nanoparticles. A ZnO/TiO2 spacer thicknesses of ~60 nm provided the greatest absorption enhancement in the Au by meeting the critical coupling condition, wherein the rate at which optical power enters the Au-(ZT)-Al structure is matched to the rate of radiative decay of the Au nanoparticles. Reflection of incident light is minimized and through conservation of energy absorption is maximized within our resonant Au structures. The physics of the critical coupling process is thoroughly explained elsewhere. 22,23,25 The final regime of spacer thickness > \sim 150 nm can be explained as forming a pseudo-Fabry-Perot cavity. While Fabry-Perot devices can enhance Au absorption by preventing reflection through destructive interference, these optical phenomena are highly dependent on the angle of incidence of incoming light and require precise spacer thickness control to maximize absorption.⁵⁰ In summary, a ZnO spacer thicknesses of ~50 nm on top of our TiO2protected Al film provided the greatest absorption improvement in Au nanostructures, both in finite element simulations and in experimental data.

2.3. Energy Band Diagram of Au-(ZT)-Al Structures. In addition to exhibiting high absorption of visible light, our MIM structures are functional and can catalyze photochemical reactions. The energy diagram of the system is shown schematically in Figure 3. At the Au-ZnO metal-semiconductor interface, an electronic potential energy barrier known as a "Schottky barrier" (Φ_B) is formed which inhibits the free flow of electrons across the interface. 3,14 Excitation of the LSPR of the Au nanoparticles can lead to nonradiative decay of the surface plasmon through Landau damping, generating hot electrons. 6,10 Hot electrons in the Au that have an energy greater than the Schottky barrier can inject into the neighboring ZnO, which mitigates recombination with the Au hot hole through physical separation of the carriers. Furthermore, the electrons injected into the ZnO conduction band maintain a more stable elevated energy and can perform reactions with a higher reduction potential than the system Fermi level. While plasmon decay excites electrons near the Au Fermi level, higher energy light can directly excite electrons from the Au d-band to the sp-band.⁸⁻¹¹ These interband excitations often generate electrons with energies just above the Fermi level which are less likely to have the necessary energy to overcome the interfacial Schottky barrier.

Using ultraviolet photoelectron spectroscopy (UPS), we quantified the ZnO and TiO_2 band positions relative to the Fermi energy level (Supporting Information, section S7). We calculated that the conduction band minimum (CBM) of our

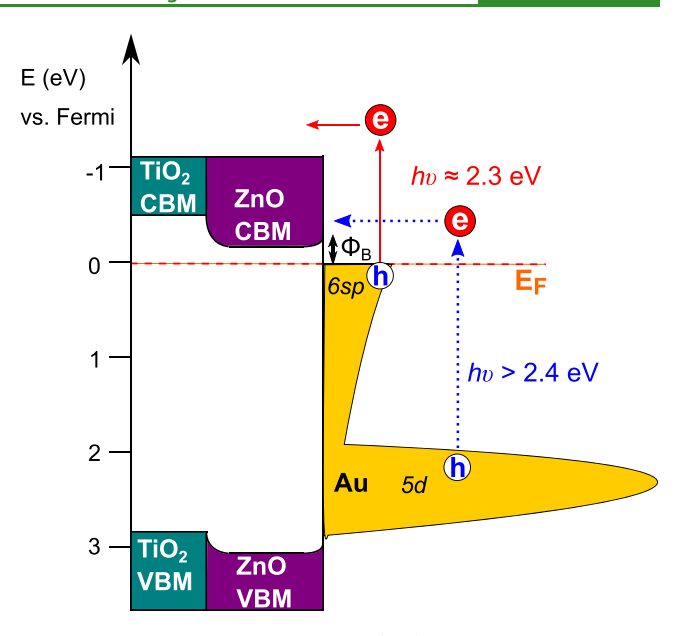


Figure 3. Band energy diagram for Au-(ZT)-Al structures and schema representing the proposed electron transfer mechanisms. Plasmon excitations lead to Landau damping for electrons near the Fermi level (red arrows) and are the main source of electron transfer studied in this work, though Au interband excitations (blue dot arrows) are dominant for light of sufficient energy (>2.4 eV).

ZnO is ~0.3 eV lower than that of the ${\rm TiO_2}$ capping layer, meaning electron migration from ZnO to ${\rm TiO_2}$ is energetically unfavorable and not expected to occur in our system. Additionally, we calculated the Schottky barrier at our Au–ZnO interface to be 0.30 \pm 0.04 eV, which is lower than most values in the literature (0.7–1.0 eV). This discrepancy may be attributed to surface defect states, ZnO crystal quality, Fermi level pinning, or barrier height inhomogeneities. S5,56

2.4. Electron Transfer Efficiency Probed with Ultrafast Pump-Probe Spectroscopy. 2.4.1. Evidence of Hot-Electron Transfer from Au to ZnO. The excitation of Au nanoparticles with photon energies near the Au LSPR produces a short-lived distribution of hot electrons in Au through Landau damping.^{6,10} Herein, a confined surface plasmon decays by exciting an electron near the Fermi level to a higher energy state of $\sim E_{\rm F} + h\omega$ within the same sp-band (i.e., an intraband transition). When Au is in contact with a semiconductor, hot electrons with a higher energy than the interfacial Schottky barrier can inject into the semiconductor conduction band, as shown in Figure 3. Alternatively, excitation of Au with energies above ~2.4 eV can excite electrons from the high-density d-band into the sp-band (i.e., interband transition). 9,10 The athermal distribution of hot electrons from Landau damping is short-lived, with previous studies reporting rapid hot electron relaxation in Au through electron–electron scattering (<200 fs) and electron–phonon coupling (\sim 1 ps). ^{51–54} Following these ultrafast relaxation processes, thermalization with the lattice cools the Au nanostructures back to the equilibrium state.

To investigate hot-electron generation and transfer within our Au-(ZT)-Al structures, we implemented pump—probe transient absorption (TA) spectroscopy. Samples were photoexcited with an ultrafast (\sim 50 fs) pump pulse and then probed following a short tunable time delay with a broadband UV—vis pulse. The excitation of electrons from one state to another induces a temporary change in absorbance as a result of

phenomena such as ground-state bleaching, photoinduced absorption, or stimulated emission. The transient response provides insight into the photoexcited electron dynamics, including hot-electron relaxation, recombination lifetime, and interfacial charge transfer rate. Pump—probe studies have also been used to determine the hot-electron injection efficiency for Au nanostructures embedded within a ${\rm TiO_2}$ matrix. The combination of TA experiments and theoretical models, such as the two-temperature model, has proven to be powerful tools to analyze fundamental hot-electron processes and their efficiencies.

We chose pump energies across the ultraviolet and visible spectra to selectively excite our sample and infer specific electronic excitations. Initially, the Au-(ZT)-Al sample was photoexcited with a 330 nm UV pump and probed from 350 to 650 nm, as shown in Figure 4a. The bleach near 366 nm was attributed to excitations in ZnO, while the bleach near 535 nm was associated with Au interband excitations. The dynamics of the transient absorption at 366 and 560 nm (Figure 4b) shows

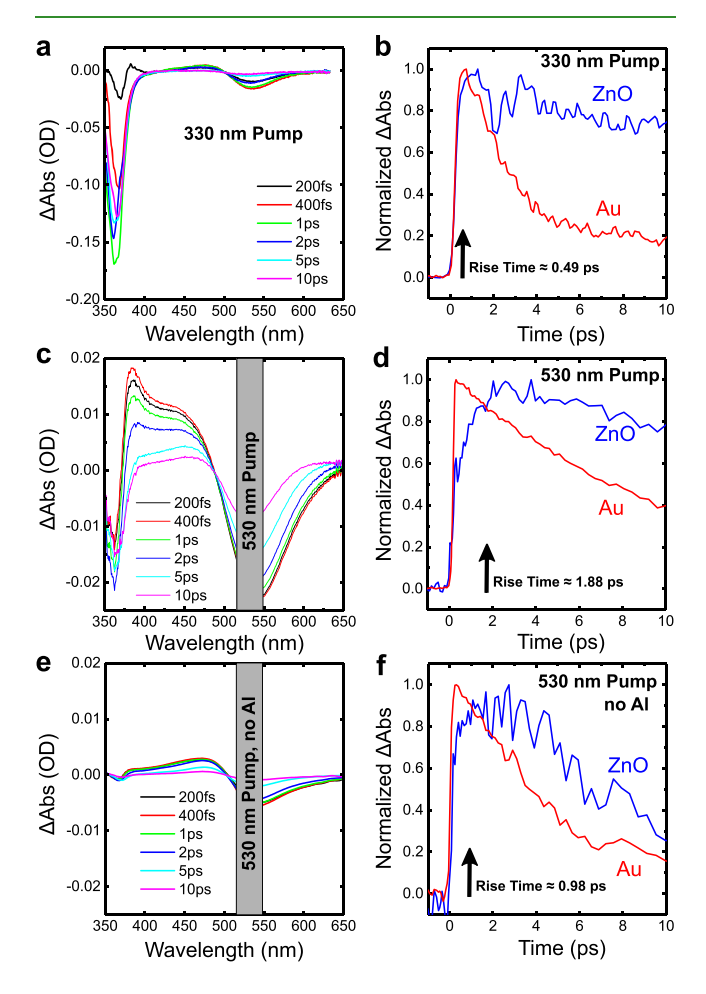


Figure 4. Time-resolved differential absorption spectra for Au-(ZT)-Al samples pumped with (a) 330 nm and (c) 530 nm light. An Au-(ZT) sample without Al was also pumped at 530 nm (e) for comparison. Normalized kinetics of transient absorption at 366 and 560 nm for these tests are provided in (b), (d), and (f). The 366 nm kinetics are attributed to electron accumulation in the ZnO conduction band, while the 560 nm signal is indicative of changes in Au. Rise times for the ZnO signal are also inset for better visualization of the indirect charge transfer into ZnO for samples pumped with visible light.

a signal rise time—defined as the time to reach 90% of the maximum absorbance change—of <500 fs for ZnO and Au since both materials can be directly photoexcited by UV light.

When pumped with visible (530 nm) light, our samples still exhibit a UV bleach which cannot be attributed to ZnO photoexcitations (as confirmed by UV-vis spectroscopy, ellipsometry, and ultrafast absorption spectroscopy in Figures S1 and S17). Instead, the UV signal arises from injection of electrons from Au excited near its LSPR (Figure 4c). We provided similar photon flux for each pump wavelength: 4.8 × 10^{14} cm^{-2} was used for UV pumps, and a flux of 2.6×10^{15} cm⁻² used in all visible pumps. The smaller magnitude of the ZnO bleach with visible excitation indicates that the electron transfer from Au is less efficient that the direct excitation of ZnO with UV photons. Under visible light, the dynamics (Figure 4d) show that the Au bleach is again nearly instantaneous, but the rise time of the ZnO peak is >3 times slower than when ZnO is directly excited with a 330 nm pump. To confirm spectral assignments, we show that 530 nm excitation of a control samples of Au on quartz show no measurable signal below 375 nm (Figure S17c). We also show that 300 nm excitation of a control samples of (ZT)-Al without Au shows no measurable signal centered around 535 nm (Figure S17f).

Samples without Al—and therefore without critical coupling of visible light into the Au resonant structures—exhibit weaker differential absorption under the same pump fluence (Figure 4e) as well as faster signal rise times (Figure 4f) compared to those of Au-(ZT)-Al samples. The rise time of the 366 nm signal for Au-(ZT)-EXG samples is still about twice that of UV-pumped samples, and electron injection is clearly observed, though the smaller signal indicates that fewer electrons have been photoexcited in Au and subsequently injected into ZnO. We speculate that the slower 366 nm signal rise time from critically coupled samples may be indicative of extended hot electron transfer from the Au due to slower thermal relaxation.

2.4.2. Extended Hot-Electron Lifetimes in Critically Coupled Samples. The ability of hot electrons to inject from Au into ZnO is dependent upon the thermalization kinetics of the system, which are in turn a function of the electronphonon (e-ph) coupling time. To determine e-ph coupling times, we pumped our samples with 530 nm light to excite the Au nanostructures at their LSPRs and probed at the same wavelength. We fit the transient absorption under varying pump fluences with Sun's two-temperature model, sa as detailed in section S6 of the Supporting Information. We assumed an electron-electron scattering time of <200 fs, which is within the range of literature values for electron scattering events in Au excited with >2 eV light. 52,53,59 The eph coupling times calculated from two-temperature fits are plotted as a function of pump power in Figure 5a. The positive trend of e-ph coupling time with pump fluence in all cases is expected, given that higher pump fluences lead to more hotelectron generation and in turn higher electronic temperatures and longer relaxation times.⁶⁰ Furthermore, the fitted lowfluence limit for e-ph coupling time for Au nanostructures is ~1.1 ps for both Al and non-Al backed samples, which matches very well with values reported in the literature.^{7,19}

Interestingly, we observed longer e-ph coupling times for critically coupled samples in comparison to samples without the Al reflector under similar pump fluences. We attribute the extended hot-electron lifetimes in critically coupled samples to

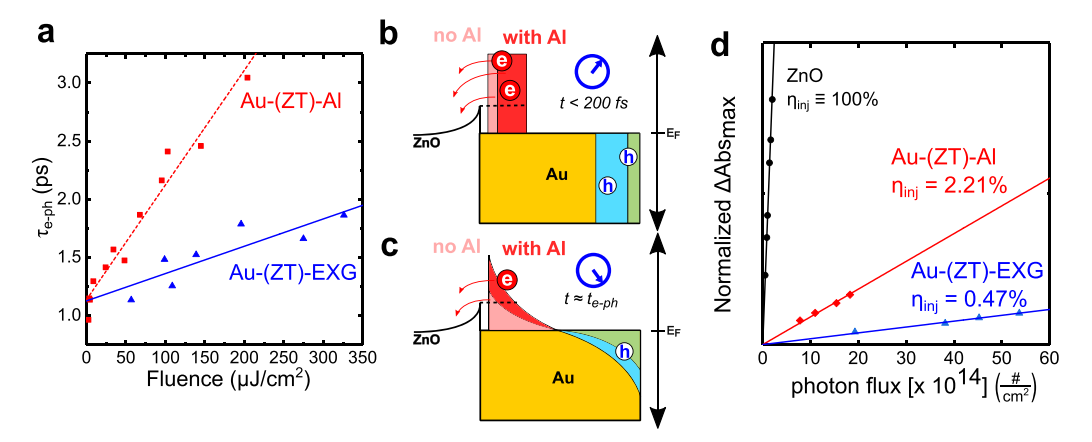


Figure 5. (a) Electron–phonon coupling times from Au-(ZT)-Al (red squares) and Au-(ZT)-EXG (blue triangles) as a function of pump fluence fitted by using Sun's two-temperature model. 53 A linear correlation was also established for both Al-backed samples (dashed red line) and samples without Al (solid blue line). (b) Schematic demonstrating benefits of critical coupling to hot electron lifetimes and injection. Immediately following Landau damping, an extended distribution of energies for electrons (red) and holes (blue) is obtained relative to $E_{\rm F}$. Electrons with enough energy can inject into ZnO within ultrafast time scales. (c) Thermal relaxation through electron–phonon interactions causes the energies of excited hot carriers to approach a Fermi–Dirac distribution. Within this time frame, hot electrons with energy greater than the Schottky barrier are still expected to be able to inject into ZnO, until further thermalization lowers the energy distribution. (d) Maximum differential absorption ($\Delta A_{\rm max}$) at the ZnO bleach vs photon flux for samples without Au pumped with UV light (black dots), and samples with Au pumped under 530 nm light, both with Al (red diamonds) and without Al (blue triangles). We applied a linear fit to all data sets and used the ratio of the fitted slopes to estimate electron injection efficiency from Au into the ZnO conduction band.

a larger population of hot electrons generated, as visualized in Figure 5b. Furthermore, we observe a strong correlation between the e-ph coupling times in Au and the ZnO rise times for samples pumped under equal fluences (Figure S16). This relation supports the previous suggestion that the 366 nm signal rise time is indicative of extended, indirect electron injection from Au into ZnO as a result of slower thermal relaxation (Figure 5c). It is also worth noting that the Au-(ZT)-Al samples exhibited slower ZnO rise times and longer Au e-ph coupling times as the excitation wavelength approached the Au LSPR.

2.4.3. Measurement of Electron Injection Efficiency. To quantify the benefits to electron injection from critical coupling, we measured the maximum change in absorbance at 366 nm corresponding to the ZnO conduction band for a range of samples and pump profiles. Using a methodology similar to Pehrsson et al., we compared the maximum differential absorption at 366 nm as a function of pump power for non-Au samples pumped with UV light to that of samples with Au under visible excitation. We assumed that ZnO would convert UV photons of energy ~3.75 eV (330 nm) to excited electrons with a quantum efficiency of 1 because ZnO has a direct bandgap of ~3.26 eV as measured by the Tauc plot (Figure S5). The fractional absorption of TiO₂ at 330 nm is calculated to be <10% and is assumed to contribute negligibly to the 366 nm peak ascribed to ZnO in the pump-probe studies. This calculation is based on the relative thickness of ZnO along with the fact that anatase TiO₂ has an indirect bandgap with weak absorption beginning only at ~3.36 eV (369 nm).

We determined the correlation parameter tying differential absorption to electron population in ZnO by pumping samples without Au with 330 nm light under a range of fluences that gave a linear trend in maximum differential absorption at 366 nm, as shown in the black data points of Figure 5d. We then performed comparative measurements on samples containing Au nanostructures pumped at 530 nm to determine the population of electrons injected into ZnO from photoexcited

Au, also shown in Figure 5d. Using the ratio of the slopes for UV-excited ZnO and visibly excited Au–ZnO, we estimated the overall electron injection efficiency ($\eta_{\rm inj}$). In the samples without Al, the hot-electron injection efficiency in ZnO was ~0.47%. While low, this efficiency fits within the estimates of previous theoretical calculations. However, for critically coupled Au-(ZT)-Al samples, the injection efficiency rose to ~2.2%, or ~5 times greater than in samples without Al. Further details regarding the calculation of injection efficiency are provided in Figure S18.

2.5. Visible-Light-Driven Generation of Hydrogen Peroxide. Improvements in the efficiency of hot-electron collection in ZnO from visible excitation of Au should also translate to an improvement in photocatalytic performance. To confirm this connection, we designed a photocatalytic microreactor for our Au-(ZT)-Al samples and measured the generation of H2O2 under visible-light irradiation. Previous studies have demonstrated the ability of UV illumination to produce superoxide from the reaction of excited electrons in the ZnO conduction band with dissolved oxygen. 61,62 The superoxide ion can then participate in various redox reactions to form hydrogen peroxide, which is the most stable of the reactive oxygen species (ROS). One notable difference in our visible-light-driven system compared to UV-driven ROS generation from ZnO is that the hole remaining in the Au nanostructures has a comparatively lower oxidation potential than that of UV-excited ZnO. The hot hole generated through Landau damping is, at most, $h\omega$ below the Fermi level (~2.3 eV for our system) while the ZnO valence band maximum (VBM) is positioned ~3.08 eV below the Fermi level (Figure \$26). The hot holes must be quenched by electrons in the surrounding environment. While deionized (DI) water has an unfavorable redox potential for single-electron donation to the Au hot hole, ethanol can be a suitable electron donor. 21,63 Therefore, we performed our reactions in a 5% (v/v) ethanolic solution. An abridged set of relevant reaction equations for this process, along with their respective redox potentials at pH 7, are provided in the following equations.⁶⁴

$$Au + h\nu \rightarrow e^{-} + h^{+} \rightarrow Au(h^{+}) - ZnO(e^{-})$$
 (1)

$$O_2 + e^- \rightarrow O_2^{*-} (-0.33 \text{ eV})$$
 (2)

$$O_2 + 2e^- + 2H^+ \rightarrow H_2O_2 (+0.68 \text{ eV})$$
 (3)

$$H_2O_2 + e^- \rightarrow OH^- + OH^* (+0.71 \text{ eV})$$
 (4)

$$O_2^{*-} + H^+ \to HO_2^* (+1.00 \text{ eV})$$
 (5)

$$CH_3CH_2OH + 2h^+ \rightarrow CH_3CHO + H_2 (+1.20 \text{ eV})$$
 (6)

$$HO_2^* + e^- + H^+ \to H_2O_2 (+1.44 \text{ eV})$$
 (7)

$$2H_2O + 2h^+ \rightarrow 2H^+ + H_2O_2 (+1.76 \text{ eV})$$
 (8)

$$H_2O + h^+ \rightarrow OH^* + H^+ (+2.74 \text{ eV})$$
 (9)

We designed our reactor to allow $6.25~\rm cm^2$ area illumination from a solar simulator and provide a uniform flow profile of reaction solution over a thin film—substrate. A schematic of our reactor in Figure 6a shows the general photocatalytic process. A solar simulator (WaveLabs Sinus 70) paired with a 450+ nm long-pass filter created an incident spectral radiation of $600~\rm W~m^{-2}$ with a profile designed to very accurately match

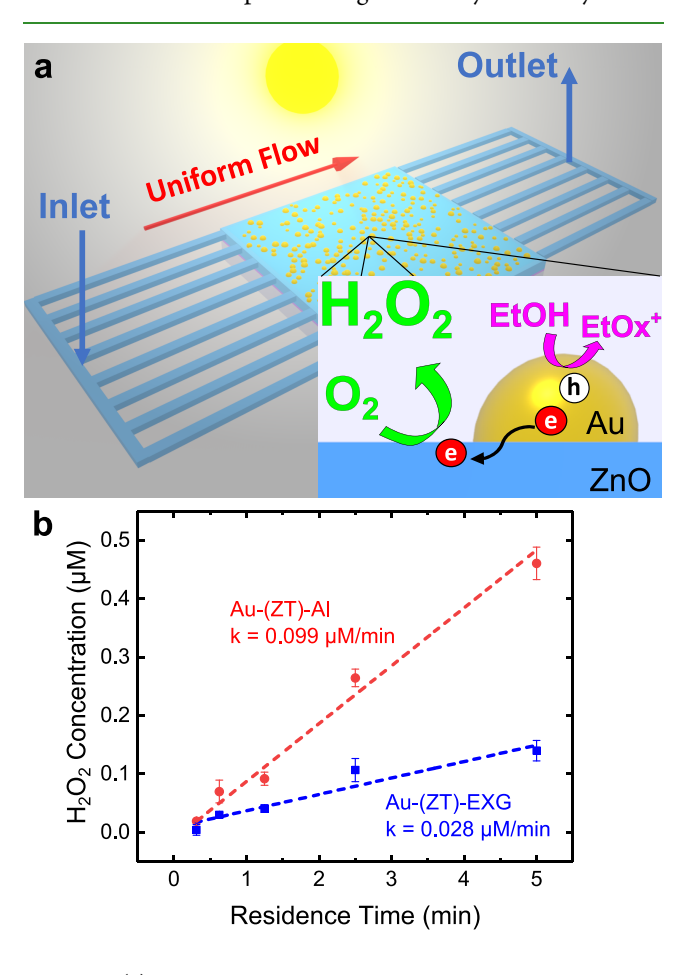


Figure 6. (a) Schematic of the microreactor system used for in situ photocatalytic H_2O_2 generation. The inset shows the flow of hot carriers at the Au–ZnO interface and the simplified overall redox reactions. (b) Photocatalytic H_2O_2 accumulation, found through the linear relation of H_2O_2 concentration generated to the microreactor flow rate, is $\sim 3.5 \times$ greater for Au-(ZT) photocatalysts with Al backing compared to those without Al.

the AM1.5G solar spectrum out to \sim 1050 nm (Figure S25). The 450 nm cutoff ensured that none of the ZnO (or TiO₂) within the sample was photoexcited and that only Au nanoparticles would be able to generate excited charge carriers. Hydrogen peroxide was quantified ex situ with the selective fluorescent probe Amplex Red.

By varying the flow rate of reaction solution in our reactor, we derived a general trend for the concentration of H₂O₂ generated with respect to residence time in the reactor. This linear relationship establishes a net rate of H₂O₂ generation, while also accounting for side reactions generating other ROS or degrading H₂O₂. These trends are shown in Figure 6b and indicate that critical coupling in our MIM structure leads to an ~3.5× improvement in photocatalytic activity under a broad visible spectrum. Control samples lacking Au nanostructures generated negligible ($<0.05 \mu M$) hydrogen peroxide at all flow rates, as did test samples of Au-(ZT)-Al or Au-(ZT)-EXG under dark conditions (Figures S19 and S20). These data support the hypothesis that an improvement in hot-electron collection efficiency in metal/semiconductor structures leads to greater photocatalytic activity under appropriate light conditions. To realize a significant increase in hot-electron collection efficiency from critical coupling for solar-driven photocatalysis, high fluence from artificial lamps or solar concentrators is likely necessary. Furthermore, the quantum efficiency of our system could likely be improved by better scavenging of the Au hot hole and improving the mass transfer of the oxygen reactant within our reactor.

Other studies have explored similar visible-light photocatalysis, although rarely with the Au-ZnO motif. The reason is simple: ZnO is not very stable in aqueous environments. In our studies, the ZnO films showed appreciable dissolution within a few hours. As such, we believe that ZnO is not suitable for long-term photocatalytic applications. For these studies, however, ZnO provided several benefits. As a direct-bandgap semiconductor, we used ZnO for room-temperature Au photodeposition, and we analyzed UV-induced charge generation in ZnO using ultrafast transient absorption spectroscopy with an assumed unity quantum efficiency. Additionally, ZnO has been shown to cause much lower adsorption and degradation of hydrogen peroxide than TiO₂, allowing for a better measure of photocatalytic activity in our 61,67,68 The Au–ZnO Schottky barrier in our samples (\sim 0.3 eV, Figure S27) is also far lower than literature values of the Schottky barrier at Au-TiO2 interfaces, thus allowing for greater hot-electron generation into the respective conduction band.^{29,55}

3. CONCLUSION

The use of an Al film to critically couple visible light to Au nanoparticles in a MIM structure provides a low-cost means of enhancing hot-electron collection in photocatalytically active devices. Compared to systems on bare glass, our critically coupled samples exhibit a 5-fold increase in visible-light absorption within Au nanoparticles, a nearly 5-fold increase in electron injection from Au to ZnO, more than double the hot-electron lifetime under 0.1 mJ cm $^{-2}$ radiant fluence, and a 3.3× improvement in the photocatalytic yield of $\rm H_2O_2$. Overall, this work highlights ability to confine electromagnetic radiation within supported plasmonic systems by using low-cost materials and lithography-free fabrication, which may prove necessary for hot-electron devices to progress from bench top models to commercialized products.

4. EXPERIMENTAL METHODS

4.1. Materials. Chemicals and materials for this work were as follows: zinc acetate dihydrate (J.T. Baker); pure ethanol (Koptec); ethanolamine (Alfa Aesar); Al (RD Mathis); aurochloric acid trihydrate (Beantown Chemical); Amplex Red (Cayman Chemical); horseradish peroxidase (Amresco/VWR); sodium phosphate monobasic and dibasic (Mallinckrodt Chemical); Decon 90 (Electron Microscopy Sciences); isopropanol (Fisher Chemicals); hydrogen peroxide, 35% w/w (BDH/VWR); and ammonium hydroxide 28–30% w/w (BDH/VWR).

4.2. Synthesis of Al, TiO₂, **ZnO**, **and Au Layers.** Corning Eagle XG glass was diced into 2.5 cm \times 2.5 cm (or 5 cm \times 5 cm) pieces and cleaned in batch by sonicating in a 4% solution of Decon 90 at 130 kHz for 30 min, followed by sonication in DI water at 130 kHz for 30 min. Glass pieces were then rinsed with isopropyl alcohol, dried with N₂, and heated at 100 °C to remove any additional residue. For Albacked samples, we mounted clean glass in a vacuum chamber where we evaporated a 5 nm Cr adhesion layer followed by a nominal 300 nm of aluminum at a rate of >100 Å/s with a starting pressure below 5 \times 10⁻⁷ Torr. Samples were removed and stored in sealed, ambient conditions for ~24 h.

We used atomic layer deposition (ALD) to apply a thin pinholefree layer of TiO₂ onto the substrates with and without an Al film. See the Supporting Information for details on our ALD procedure. We used a sol-gel approach to synthesize our ZnO films. In short, we mixed a 1.0 M zinc acetate and 1.0 M ethanolamine in pure ethanol. We mixed this solution vigorously for 2 h and then allowed it to sit for at least 24 h in a sealed centrifuge tube before use. The ZnO sol-gel had a shelf life of months, and we replaced it every 4 weeks. We fabricated a 50 nm thick layer of ZnO by pipetting the ZnO sol onto a sample surface with just enough volume to cover the surface entirely. We then spun the sample at 3000 rpm for 30 s and immediately annealed on a hot plate at 400 °C in ambient conditions. Thicker and thinner ZnO layers were formed by spinning multiple layers, adjusting the spinning conditions, and diluting the sol-gel with ethanol before spinning. We deposited Au nanoparticles on the ZnO films through photodeposition, a process which is described further in the Supporting Information.

4.3. Optical Characterization: Absorbance, Reflection, and Ellipsometry. We determined the material absorbance of the samples by mounting them in an integrating sphere at 10° incidence within a PerkinElmer Lambda 900 UV—vis—NIR spectrophotometer. The detector collected all light that was scattered or transmitted from a sample; thus, the fraction of light absorbed by the sample was that which was not detected (i.e., A = 1 — fraction detected = 1 - S - T). For samples with ZnO or TiO₂, we observed the semiconductor band edge within the UV region, and the actual band gap estimated via a Tauc plot.

We determined the wavelength-dependent complex dielectric constants of the thin films (Au, Al, TiO₂, and ZnO) using a spectroscopic ellipsometer (J.A. Woollam RC2) operating at 55°, 65°, and 75°. Films were deposited on RCA-cleaned silicon substrates, and we fit the Ψ/Δ information according to the film characteristics. For ZnO and TiO₂, we applied a Cauchy dispersion model in their respective transparent regions with an iterative wavelength expansion fit used to estimate the material dielectric constants from 230 to 2500 nm with a minimum mean standard error (MSE). For Au and Al, a B-spline model based on bulk metal properties was used to measure their wavelength-dependent dielectric constants. The data collected fits very well with previously reported optical data on these materials. We used a reflectometer (FILMetric F20) to quickly confirm the thickness of TiO₂ and ZnO films after spin-coating using the dielectric constants collected via spectroscopic ellipsometry.

We describe further material characterization in the Supporting Information.

4.4. Ultrafast Pump—Probe Spectroscopy. We conducted femtosecond transient absorption/reflection measurements using a Helios spectrometer. We used a transmission setup for non-Al samples and reflection setup for the samples with Al. The output of

regeneratively amplified Ti:sapphire laser (Coherent Libra, 50 fs, 1 kHz, 3.5 W) was split to generate the pump and probe beams. The pump beam wavelength was selected by using an optical parametric amplifier. A broad-band white-light continuum (WLC) probe from 340 to 700 nm was generated by focusing and attenuating an 800 nm pulse into a CaF₂ crystal window. The WLC was then split to detector and reference channels to correct for any fluctuations. We spatially overlapped the pump and probe beams at the sample position, and we measured the transient absorption/reflection signal using a synchronized chopper (500 Hz) at a sequence of pump–probe time delays controlled by an optical delay stage. We recorded the transient absorption data as $\Delta A = -\log\left(\frac{I_{\rm ex,T}}{I_0,T}\right)$, where $I_{\rm ex,T}$ is the intensity of the transmitted probe of the excited sample and $I_{0,T}$ is the intensity of the transmitted probe prior to photoexcitation.

We provide further information about pump—probe studies in the Supporting Information.

4.5. Photocatalysis Studies. To quantify the amount of hydrogen peroxide generated by our samples under visible light, we used the selective probe Amplex Red in the presence of horseradish peroxidase. First, a solution of Amplex Red was made by dissolving the powder precursor in DMS to a concentration of 10 mM. We dissolved horseradish peroxidase to a concentration of (300 mU mL⁻¹) in a 7.4 pH phosphate buffer solution (0.1 M) in DI water, and then the DMS-dissolved Amplex Red was added to a final concentration of 30 µM to form an activate reaction solution (RS +). Precursors and RS+ were stored long term in the dark at -20 °C. Before use, a solution of RS+ was thawed at 4 °C in the dark and then kept in the dark on ice for the remainder of tests. We made an H₂O₂ standard curve by serial dilution of stock (30% w/w) H₂O₂ in DI water to 150 μM and then diluting in 5% EtOH to various concentrations up to 2 mL. To this $H_2\bar{O}_2$ solution, 1 mL of RS+ was added and held for 5 min to allow for all the H2O2 to react with Amplex Red. We then measured the solution fluorescence in a spectrofluorometer (PTI QM 40) with an excitation wavelength of 520 nm and an emission of 590 nm. In this way, we can linearly correlate the sample fluorescence with >0.99 r^2 correlation for concentrations of H_2O_2 up to ~1.5 μ M. Higher concentrations of H₂O₂ were determined by diluting the original H₂O₂ solution by 10× in 5% ethanol before the 1 mL addition of RS+ and then multiplying the result by a corresponding factor of 10.

We designed a microreactor to provide a uniform flow profile of reaction solution (5% ethanol in DI water) across the surface of a 5 cm \times 5 cm sample. The volume under illumination in the reaction chamber was 1.25 cm³. We used a syringe pump (Harvard Apparatus Model 22) to provide reactants at a uniform flow rate. We collected the effluent every 2 mL in small tubes, to which we added 1 mL of RS + to measure the resulting fluorescence and respective $\rm H_2O_2$ concentration. We provided a constant illumination of 600 W m $^{-2}$ with a WaveLabs Sinus 70 solar simulator with a 450+ nm long-pass filter applied above the microreactor viewport to allow only visible + NIR wavelengths of light.

ASSOCIATED CONTENT

Solution Supporting Information

The Supporting Information is available free of charge at https://pubs.acs.org/doi/10.1021/acsami.0c00825.

Additional experimental and simulation methods; optical data; XRD and Scherrer equation to estimate ZnO grain size; Au photodeposition and nanoparticle size analysis; ICP-OES measurements of Au loading; additional pump—probe data; photocatalytic control tests, UPS measurements for band energy positions (PDF)

Tabulated optical data for Al, ZnO, and TiO₂ (TXT)

AUTHOR INFORMATION

Corresponding Author

Kevin M. McPeak — Gordon and Mary Cain Department of Chemical Engineering, Louisiana State University, Baton Rouge, Louisiana 70803, United States; orcid.org/0000-0002-2766-104X; Email: kmcpeak@lsu.edu

Authors

- Daniel E. Willis Gordon and Mary Cain Department of Chemical Engineering, Louisiana State University, Baton Rouge, Louisiana 70803, United States; orcid.org/0000-0003-3133-2297
- Mohammad M. Taheri Department of Chemical and Biological Engineering, Drexel University, Philadelphia, Pennsylvania 19104, United States; orcid.org/0000-0001-9121-0078
- Orhan Kizilkaya Louisiana State University Center for Advanced Microstructures & Devices, Baton Rouge, Louisiana 70806, United States
- Tiago R. Leite Gordon and Mary Cain Department of Chemical Engineering, Louisiana State University, Baton Rouge, Louisiana 70803, United States
- Laibao Zhang Gordon and Mary Cain Department of Chemical Engineering, Louisiana State University, Baton Rouge, Louisiana 70803, United States; ◎ orcid.org/0000-0002-2325-5124
- **Tochukwu Ofoegbuna** Gordon and Mary Cain Department of Chemical Engineering, Louisiana State University, Baton Rouge, Louisiana 70803, United States
- Kunlun Ding Gordon and Mary Cain Department of Chemical Engineering, Louisiana State University, Baton Rouge, Louisiana 70803, United States; ⊚ orcid.org/0000-0002-3676-3814
- James A. Dorman Gordon and Mary Cain Department of Chemical Engineering, Louisiana State University, Baton Rouge, Louisiana 70803, United States; ⊙ orcid.org/0000-0002-3248-7752
- Jason B. Baxter Department of Chemical and Biological Engineering, Drexel University, Philadelphia, Pennsylvania 19104, United States; oorcid.org/0000-0001-8702-3915

Complete contact information is available at: https://pubs.acs.org/10.1021/acsami.0c00825

Notes

The authors declare no competing financial interest.

ACKNOWLEDGMENTS

We thank Nick S. Lombardo for his assistance in designing and building the microreactor, Sara K. F. Stofela for training on the thermal evaporator, Gyeong Min Yoo for synthesizing ZnO films, Justin Hayes for photodeposition of Au nanoparticles, Luis Manuel for scanning electron microscopy, and Prof. Chris Arges for providing access to his spin coater. D.E.W. acknowledges support from the State of Louisiana Board of Regents through their Flagship Graduate award. K.M.M. acknowledges support from the BASF Sustainable Living Laboratory at Louisiana State University. J.B.B. and M.T. acknowledge support from the National Science Foundation (Grant CHE-1708991).

REFERENCES

- (1) Clavero, C. Plasmon-induced hot-electron generation at nanoparticle/metal-oxide interfaces for photovoltaic and photocatalytic devices. *Nat. Photonics* **2014**, *8*, 95.
- (2) Linic, S.; Christopher, P.; Ingram, D. B. Plasmonic-metal nanostructures for efficient conversion of solar to chemical energy. *Nat. Mater.* **2011**, *10*, 911.
- (3) Tian, Y.; Tatsuma, T. Mechanisms and Applications of Plasmon-Induced Charge Separation at TiO_2 Films Loaded with Gold Nanoparticles. J. Am. Chem. Soc. 2005, 127 (20), 7632–7637.
- (4) Zhang, X.; Chen, Y. L.; Liu, R.-S.; Tsai, D. P. Plasmonic photocatalysis. *Rep. Prog. Phys.* **2013**, *76* (4), No. 046401.
- (5) Maier, S. A. Plasmonics: Fundamentals And Applications; Springer: New York, 2007; p 245.
- (6) Brongersma, M. L.; Halas, N. J.; Nordlander, P. Plasmon-induced hot carrier science and technology. *Nat. Nanotechnol.* **2015**, 10, 25.
- (7) Furube, A.; Du, L.; Hara, K.; Katoh, R.; Tachiya, M. Ultrafast Plasmon-Induced Electron Transfer from Gold Nanodots into ${\rm TiO_2}$ Nanoparticles. *J. Am. Chem. Soc.* **2007**, 129 (48), 14852–14853.
- (8) Manjavacas, A.; Liu, J. G.; Kulkarni, V.; Nordlander, P. Plasmon-Induced Hot Carriers in Metallic Nanoparticles. *ACS Nano* **2014**, 8 (8), 7630–7638.
- (9) Besteiro, L. V.; Kong, X.-T.; Wang, Z.; Hartland, G.; Govorov, A. O. Understanding Hot-Electron Generation and Plasmon Relaxation in Metal Nanocrystals: Quantum and Classical Mechanisms. *ACS Photonics* **2017**, *4* (11), 2759–2781.
- (10) Khurgin, J. B. How to deal with the loss in plasmonics and metamaterials. *Nat. Nanotechnol.* **2015**, *10*, *2*.
- (11) Bohren, C. F.; Huffman, D. R. Absorption and Scattering of Light by Small Particles; Wiley: New York, 1983.
- (12) Tian, Y.; Tatsuma, T. Plasmon-induced photoelectrochemistry at metal nanoparticles supported on nanoporous TiO₂. *Chem. Commun.* **2004**, *16*, 1810–1811.
- (13) Kamat, P.; Photophysical, V. Photochemical and Photocatalytic Aspects of Metal Nanoparticles. *J. Phys. Chem. B* **2002**, *106* (32), 7729–7744.
- (14) Tung, R. T. The physics and chemistry of the Schottky barrier height. *Appl. Phys. Rev.* **2014**, *1* (1), No. 011304.
- (15) Knight, M. W.; Sobhani, H.; Nordlander, P.; Halas, N. J. Photodetection with Active Optical Antennas. *Science* **2011**, 332 (6030), 702.
- (16) Leenheer, A. J.; Narang, P.; Lewis, N. S.; Atwater, H. A. Solar energy conversion via hot electron internal photoemission in metallic nanostructures: Efficiency estimates. *J. Appl. Phys.* **2014**, *115* (13), 134301.
- (17) White, T. P.; Catchpole, K. R. Plasmon-enhanced internal photoemission for photovoltaics: Theoretical efficiency limits. *Appl. Phys. Lett.* **2012**, *101* (7), No. 073905.
- (18) Ross, R. T.; Nozik, A. J. Efficiency of hot-carrier solar energy converters. J. Appl. Phys. 1982, 53 (5), 3813–3818.
- (19) Ratchford, D. C.; Dunkelberger, A. D.; Vurgaftman, I.; Owrutsky, J. C.; Pehrsson, P. E. Quantification of Efficient Plasmonic Hot-Electron Injection in Gold Nanoparticle—TiO₂ Films. *Nano Lett.* **2017**, *17* (10), 6047–6055.
- (20) Ho, K. H. W.; Shang, A.; Shi, F.; Lo, T. W.; Yeung, P. H.; Yu, Y. S.; Zhang, X.; Wong, K.-y.; Lei, D. Y. Plasmonic Au/ TiO₂-Dumbbell-On-Film Nanocavities for High-Efficiency Hot-Carrier Generation and Extraction. *Adv. Funct. Mater.* **2018**, 28 (34), 1800383.
- (21) Tsukamoto, D.; Shiro, A.; Shiraishi, Y.; Sugano, Y.; Ichikawa, S.; Tanaka, S.; Hirai, T. Photocatalytic H₂O₂ Production from Ethanol/O2 System Using TiO₂ Loaded with Au–Ag Bimetallic Alloy Nanoparticles. *ACS Catal.* **2012**, 2 (4), 599–603.
- (22) Ng, C.; Wesemann, L.; Panchenko, E.; Song, J.; Davis, T. J.; Roberts, A.; Gómez, D. E. Plasmonic Near-Complete Optical Absorption and Its Applications. *Adv. Opt. Mater.* **2019**, *7* (14), 1801660.
- (23) Chen, H.-T. Interference theory of metamaterial perfect absorbers. *Opt. Express* **2012**, *20* (7), 7165–7172.

- (24) Hägglund, C.; Zeltzer, G.; Ruiz, R.; Thomann, I.; Lee, H.-B.-R.; Brongersma, M. L.; Bent, S. F. Self-Assembly Based Plasmonic Arrays Tuned by Atomic Layer Deposition for Extreme Visible Light Absorption. *Nano Lett.* **2013**, *13* (7), 3352–3357.
- (25) Yoon, J.; Seol, K. H.; Song, S. H.; Magnusson, R. Critical coupling in dissipative surface-plasmon resonators with multiple ports. *Opt. Express* **2010**, *18* (25), 25702–25711.
- (26) Xiao, Q.; Connell, T. U.; Cadusch, J. J.; Roberts, A.; Chesman, A. S. R.; Gómez, D. E. Hot-Carrier Organic Synthesis via the Near-Perfect Absorption of Light. *ACS Catal.* **2018**, 8 (11), 10331–10339.
- (27) Berean, K. J.; Sivan, V.; Khodasevych, I.; Boes, A.; Della Gaspera, E.; Field, M. R.; Kalantar-Zadeh, K.; Mitchell, A.; Rosengarten, G. Laser-Induced Dewetting for Precise Local Generation of Au Nanostructures for Tunable Solar Absorption. *Adv. Opt. Mater.* **2016**, *4* (8), 1247–1254.
- (28) Harutyunyan, H.; Martinson, A. B. F.; Rosenmann, D.; Khorashad, L. K.; Besteiro, L. V.; Govorov, A. O.; Wiederrecht, G. P. Anomalous ultrafast dynamics of hot plasmonic electrons in nanostructures with hot spots. *Nat. Nanotechnol.* **2015**, *10*, 770.
- (29) Fang, Y.; Jiao, Y.; Xiong, K.; Ogier, R.; Yang, Z.-J.; Gao, S.; Dahlin, A. B.; Käll, M. Plasmon Enhanced Internal Photoemission in Antenna-Spacer-Mirror Based Au/ TiO₂ Nanostructures. *Nano Lett.* **2015**, *15* (6), 4059–4065.
- (30) Govorov, A. O.; Zhang, H.; Gun'ko, Y. K. Theory of Photoinjection of Hot Plasmonic Carriers from Metal Nanostructures into Semiconductors and Surface Molecules. *J. Phys. Chem. C* **2013**, 117 (32), 16616–16631.
- (31) Lee, K.-T.; Seo, S.; Guo, L. J. High-Color-Purity Subtractive Color Filters with a Wide Viewing Angle Based on Plasmonic Perfect Absorbers. *Adv. Opt. Mater.* **2015**, 3 (3), 347–352.
- (32) Lee, J.; Mubeen, S.; Ji, X.; Stucky, G. D.; Moskovits, M. Plasmonic Photoanodes for Solar Water Splitting with Visible Light. *Nano Lett.* **2012**, *12* (9), 5014–5019.
- (33) Henzie, J.; Lee, J.; Lee, M. H.; Hasan, W.; Odom, T. W. Nanofabrication of Plasmonic Structures. *Annu. Rev. Phys. Chem.* **2009**, *60* (1), 147–165.
- (34) Aluminum Prices and Aluminum Price Charts; http://www.infomine.com/investment/metal-prices/aluminum/ (accessed November 15, 2019).
- (35) Spot Price of Gold; https://goldprice.com/gold-spot-price/(accessed November 15, 2019).
- (36) Edley, M. E.; Li, S.; Guglietta, G. W.; Majidi, H.; Baxter, J. B. Ultrafast Charge Carrier Dynamics in Extremely Thin Absorber (ETA) Solar Cells Consisting of CdSe-Coated ZnO Nanowires. *J. Phys. Chem. C* **2016**, *120* (35), 19504–19512.
- (37) Berera, R.; van Grondelle, R.; Kennis, J. T. M. Ultrafast transient absorption spectroscopy: principles and application to photosynthetic systems. *Photosynth. Res.* **2009**, *101* (2), 105–118.
- (38) Bunker, B. C.; Nelson, G. C.; Zavadil, K. R.; Barbour, J. C.; Wall, F. D.; Sullivan, J. P.; Windisch, C. F.; Engelhardt, M. H.; Baer, D. R. Hydration of Passive Oxide Films on Aluminum. *J. Phys. Chem. B* **2002**, *106* (18), 4705–4713.
- (39) Grunberg, L.; Wright, K. H. R. Russell Effect on Evaporated Metal Films. *Nature* **1952**, *170* (4324), 456–457.
- (40) Scherrer, P. Bestimmung der inneren Struktur und der Größe von Kolloidteilchen mittels Röntgenstrahlen. In *Kolloidchemie Ein Lehrbuch*; Zsigmondy, R., Ed.; Springer: Berlin, 1912; pp 387–409.
- (41) Patterson, A. L. The Scherrer Formula for X-Ray Particle Size Determination. *Phys. Rev.* **1939**, *56* (10), 978–982.
- (42) Fernando, J. F. S.; Shortell, M. P.; Noble, C. J.; Harmer, J. R.; Jaatinen, E. A.; Waclawik, E. R. Controlling Au Photodeposition on Large ZnO Nanoparticles. *ACS Appl. Mater. Interfaces* **2016**, 8 (22), 14271–14283.
- (43) Halas, N. J.; Lal, S.; Chang, W.-S.; Link, S.; Nordlander, P. Plasmons in Strongly Coupled Metallic Nanostructures. *Chem. Rev.* **2011**, *111* (6), 3913–3961.
- (44) Cushman, C. V.; Sturgell, B. A.; Martin, A. C.; Lunt, B. M.; Smith, N. J.; Linford, M. R. Eagle XG® glass, optical constants from

- 230 to 1690 nm (0.73 5.39 eV) by spectroscopic ellipsometry. *Surf. Sci. Spectra* **2016**, 23 (1), 55–60.
- (45) Ehrenreich, H.; Philipp, H. R.; Segall, B. Optical Properties of Aluminum. *Phys. Rev.* **1963**, *132* (5), 1918–1928.
- (46) Balamurugan, B.; Maruyama, T. Evidence of an enhanced interband absorption in Au nanoparticles: Size-dependent electronic structure and optical properties. *Appl. Phys. Lett.* **2005**, 87 (14), 143105
- (47) Derkachova, A.; Kolwas, K.; Demchenko, I. Dielectric Function for Gold in Plasmonics Applications: Size Dependence of Plasmon Resonance Frequencies and Damping Rates for Nanospheres. *Plasmonics* **2016**, *11* (3), 941–951.
- (48) Qu, C.; Ma, S.; Hao, J.; Qiu, M.; Li, X.; Xiao, S.; Miao, Z.; Dai, N.; He, Q.; Sun, S.; Zhou, L. Tailor the Functionalities of Metasurfaces Based on a Complete Phase Diagram. *Phys. Rev. Lett.* **2015**, *115* (23), 235503.
- (49) Ogawa, S.; Kimata, M. Metal-Insulator-Metal-Based Plasmonic Metamaterial Absorbers at Visible and Infrared Wavelengths: A Review. *Materials* **2018**, *11* (3), 458.
- (50) Kenanakis, G.; Mavidis, C. P.; Vasilaki, E.; Katsarakis, N.; Kafesaki, M.; Economou, E. N.; Soukoulis, C. M. Perfect absorbers based on metal—insulator—metal structures in the visible region: a simple approach for practical applications. *Appl. Phys. A: Mater. Sci. Process.* **2017**, *123* (1), *77*.
- (51) Link, S.; Burda, C.; Wang, Z. L.; El-Sayed, M. A. Electron dynamics in gold and gold—silver alloy nanoparticles: The influence of a nonequilibrium electron distribution and the size dependence of the electron—phonon relaxation. *J. Chem. Phys.* **1999**, *111* (3), 1255—1264.
- (52) Groeneveld, R. H. M.; Sprik, R.; Lagendijk, A. Femtosecond spectroscopy of electron-electron and electron-phonon energy relaxation in Ag and Au. *Phys. Rev. B: Condens. Matter Mater. Phys.* 1995, 51 (17), 11433–11445.
- (53) Sun, C. K.; Vallée, F.; Acioli, L. H.; Ippen, E. P.; Fujimoto, J. G. Femtosecond-tunable measurement of electron thermalization in gold. *Phys. Rev. B: Condens. Matter Mater. Phys.* **1994**, *50* (20), 15337–15348.
- (54) Watanabe, K.; Menzel, D.; Nilius, N.; Freund, H.-J. Photochemistry on Metal Nanoparticles. *Chem. Rev.* **2006**, *106* (10), 4301–4320.
- (55) Brillson, L. J.; Lu, Y. ZnO Schottky barriers and Ohmic contacts. J. Appl. Phys. 2011, 109 (12), 121301.
- (56) Das, S. N.; Choi, J.-H.; Kar, J. P.; Moon, K.-J.; Lee, T. I.; Myoung, J.-M. Junction properties of Au/ZnO single nanowire Schottky diode. *Appl. Phys. Lett.* **2010**, *96* (9), No. 092111.
- (57) Baxter, J. B.; Richter, C.; Schmuttenmaer, C. A. Ultrafast Carrier Dynamics in Nanostructures for Solar Fuels. *Annu. Rev. Phys. Chem.* **2014**, 65 (1), 423–447.
- (58) Tagliabue, G.; DuChene, J. S.; Abdellah, M.; Habib, A.; Hattori, Y.; Zheng, K.; Canton, S. E.; Gosztola, D. J.; Cheng, W.-H.; Sundararaman, R.; Sa, J.; Atwater, H. A. Ultrafast Studies of Hot-Hole Dynamics in Au/p-GaN Heterostructures. arXiv.org e-Print archive, 2018; p arXiv:1810.04238.
- (59) Ortolani, M.; Mancini, A.; Budweg, A.; Garoli, D.; Brida, D.; de Angelis, F. Pump-probe spectroscopy study of ultrafast temperature dynamics in nanoporous gold. *Phys. Rev. B: Condens. Matter Mater. Phys.* **2019**, 99 (3), No. 035435.
- (60) Voisin, C.; Del Fatti, N.; Christofilos, D.; Vallée, F. Ultrafast Electron Dynamics and Optical Nonlinearities in Metal Nanoparticles. *J. Phys. Chem. B* **2001**, *105* (12), 2264–2280.
- (61) Sahel, K.; Elsellami, L.; Mirali, I.; Dappozze, F.; Bouhent, M.; Guillard, C. Hydrogen peroxide and photocatalysis. *Appl. Catal., B* **2016**, *188*, 106–112.
- (62) Kormann, C.; Bahnemann, D. W.; Hoffmann, M. R. Photocatalytic production of hydrogen peroxides and organic peroxides in aqueous suspensions of titanium dioxide, zinc oxide, and desert sand. *Environ. Sci. Technol.* 1988, 22 (7), 798–806.
- (63) Al-Azri, Z. H. N.; Chen, W.-T.; Chan, A.; Jovic, V.; Ina, T.; Idriss, H.; Waterhouse, G. I. N. The roles of metal co-catalysts and

- reaction media in photocatalytic hydrogen production: Performance evaluation of M/ TiO₂ photocatalysts (M = Pd, Pt, Au) in different alcohol-water mixtures. J. Catal. 2015, 329, 355-367.
- (64) Wang, C.; Zhang, X.; Liu, Y. Promotion of multi-electron transfer for enhanced photocatalysis: A review focused on oxygen reduction reaction. *Appl. Surf. Sci.* **2015**, 358, 28–45. (65) Wood, P. M. The potential diagram for oxygen at pH 7.
- Biochem. J. 1988, 253 (1), 287-289.
- (66) Wardman, P. Reduction Potentials of One-Electron Couples Involving Free Radicals in Aqueous Solution. J. Phys. Chem. Ref. Data 1989, 18 (4), 1637–1755.
- (67) Boonstra, A. H.; Mutsaers, C. A. H. A. Adsorption of hydrogen peroxide on the surface of titanium dioxide. J. Phys. Chem. 1975, 79 (18), 1940–1943.
- (68) Li, X.; Chen, C.; Zhao, J. Mechanism of Photodecomposition of H₂O₂ on TiO₂ Surfaces under Visible Light Irradiation. Langmuir 2001, 17 (13), 4118-4122.